Domain morphology and electro-optic effect in Si-integrated epitaxial math xmlns="http://www.w3.org/1998/Math/MathML">mrow>mi>BaTi/mi>msub>mi mathvariant="normal">O/mi>mn>3/mn>/msub>/mrow>/math> films

Wente Li, Chad M. Landis, and Alexander A. Demkov

Phys. Rev. Materials **6**, 095203 — Published 20 September 2022

DOI: 10.1103/PhysRevMaterials.6.095203

Domain morphology and electro-optic effect in Si-integrated epitaxial $BaTiO_3$ films

Wente Li[1], Chad M. Landis[2] and Alexander A. Demkov[a1]

[1]Department of Physics, The University of Texas, Austin, Texas 78712, USA

[2]Department of Aerospace Engineering and Engineering Mechanics, The University of Texas, Austin, Texas 78712, USA

Abstract

Ferroelectric $BaTiO_3$ thin films epitaxially integrated on Si is an emergent platform for fabricating integrated electro-optical modulators using the linear electro-optic effect for applications in silicon photonics. These devices hold great promise for optical neuromorphic and quantum computing. Understanding the domain morphology of such films is essential for building ultra-fast, ultra-low power electro-optic modulators. However, the domain morphology of the film is marked by significant complexity and our knowledge of it and its relation to the electro-optic response in epitaxial thin films is limited. In this paper, we use a phase field model implemented within the finite element method to map domain morphologies. The corresponding electro-optic response is also discussed.

I. Introduction

Recent advances in developing Si-integrated electro-optical (EO) devices offer a unique opportunity to overcome the limitations of pure electronic devices by using ultrafast optics controlled by ultralow-power electronics. The renaissance of silicon photonics owes much to the technology's natural compatibility with the current Si-based semiconductor manufacturing processes, combined with the promise of a beyond-Moore's Law paradigm. Indeed, Si photonic devices find applications in optical interconnects [1, 2], optical reservoirs [3] and, more generally, optical neuromorphic computing [4-7], as well as in optical quantum information processing [8, 9]. EO modulators are the essential enabling component of this photonic technology, offering advantages of simplicity, speed and low power [10]. EO modulators using the Pockels effect are under intensive research and have very high modulation speed and reasonably low loss [11-15]. Several other EO-active materials are also being considered for integrated photonics, such as commercially used ferroelectric $LiNbO_3$ (LNO) [16] and organic materials [17, 18].

Ferroelectric perovskite oxide $BaTiO_3$ (BTO) is among the most promising candidates for integrated Si photonics [19, 20]. The largest component of the Pockels tensor $\boldsymbol{r_{42}}$ of bulk BTO is ~1300 pm/V [21], and in thin films, has been reported to be as high as ~923 pm/V [12], much larger than LNO's ~30 pm/V [22] or strained Si's 1.7 pm/V (unstrained Si is centrosymmetric and therefore does not exhibit the Pockels effect) [23]. Integration of

---

[a] demkov@physics.utexas.edu

LNO on Si is quite difficult and can be done only for relatively small wafers [16, 24], limiting its applications in Si photonics. On the other hand, after the pioneering discovery of epitaxial crystalline oxides on Si [20, 25, 26], the mature process of wafer scale epitaxial integration of BTO on Si substrate via a $SrTiO_3$ (STO) buffer layer has been developed [20, 27]. This has enabled the fabrication of Pockels-effect-based EO modulators compatible with Si photonics [12-14]. Compared with organic materials, BTO is much more thermally stable and can operate at a wider range of temperatures. Low power switching and high-speed modulation using Si-integrated BTO thin films at room [12] and cryogenic temperatures [11] have been demonstrated, suggesting that BTO-based EO modulators can also be used for quantum computation at ultralow temperatures [20].

Bulk BTO is a prototypical ferroelectric material, found in the tetragonal (T) phase between 8°C and 125°C; in the orthorhombic (O) phase between -71°C and 8°C; and in the rhombohedral (R) phase below -71°C, while above 125°C, it is a cubic paraelectric material. The transitions between these phases are sensitive to strain [28]. While at room temperature, BTO is expected to be in the tetragonal ***P4mm*** phase (T-phase), in epitaxial BTO thin films on STO/Si substrate, the electro-mechanical conditions can strongly influence the phase composition [29]. This results in highly complex domain morphologies in epitaxial films [30]. Because BTO is also piezoelectric, applying an external electric field causes changes in the BTO polarization and strain field distributions [31, 32]. As pointed out in Ref. [4], the Pockels coefficient is a tensor closely related to both crystallographic and polarization distributions. Therefore, it is beneficial to analyze the crystallographic and polarization variations in BTO thin films simultaneously under different external conditions and establish their connection with Pockels coefficients.

Despite the astounding progress in EO modulation achieved with epitaxial BTO/STO/Si stacks [12], epitaxial BTO thin film effective Pockels coefficients are always smaller than that of bulk BTO [19]. Several elements may be responsible for the difference between the effective Pockels coefficient in a BTO thin film and in bulk, e.g., the coexistence of domains of different orientations or the mere presence of domain walls [33]. Experimentally, according to X-ray diffraction (XRD) and scanning transmission electron microscopy (STEM), Si-integrated BTO films at room temperature exhibit so-called c-domains (with the long axis of the T-phase along the out-of-plane growth direction) near the BTO/STO interface due to compressive strain. However, the a-domain (the long axis of T-phase being in-plane) is found near the BTO top surface due to the relaxation of BTO strain and suppression of the out-of-plane polarization thanks to the open-circuit boundary condition [34]. This domain reorientation is shown in Fig. 1 (a) and (b). To detect the polarization variations of BTO, one can utilize second harmonic generation [31, 35, 36] or piezoresponse force microscopy (PFM) [37]. In principle, the crystallographic and polarization structures of BTO are defined differently, even though they are strongly coupled with each other and completely overlap in bulk BTO. The crystallographic structure is determined by the Ba atoms position while polarization by Ti and oxygen atoms displacement. In the literature, there remains an ambiguity when one discusses the polar and crystallographic variations across the film, because some authors refer to the crystallographic structure via STEM and others refer to polarization structure via PFM or STEM. Jia et. al. [38] use STEM to analyze both the crystallographic and polarization structures of $PbZr_{0.2}Ti_{0.8}O_3$ thin films. Li et. al. [39] use STEM to analyze both the crystallographic and polarization structures of $PbTiO_3$ thin films. One can clearly observe the differences between the crystallographic and polarization variations across the film, especially at the domain wall. To the best of our knowledge, there is no such data for BTO films.

Usually, EO measurements lack the spatial resolution needed to explore the effects of structural variations [34]. This makes the precise determination of the Pockels tensor components difficult, and instead one uses an "effective" Pockels coefficient to describe the thin film EO response. We currently lack the mapping among the polarization, crystallographic and Pockels coefficient variations in Si-integrated BTO thin films [11, 40], which requires extremely high spatial resolution (~1 nm scale) measurements. These variations influence the effective Pockels coefficient of the film, though not necessarily in the same manner. The ambiguity of the connection between the high-resolution domain morphologies and the effective Pockels coefficient limits our ability to optimize the BTO thin film EO response e.g., by varying growth conditions. In the absence of experimental measurements, it is clear that numerical simulations of the domain structure would be beneficial. On the theoretical side, density functional theory (DFT) gives accurate descriptions of bulk BTO [41, 42]. BTO surface structure has been studies using DFT with relatively small simulation cells [43, 44]. However, it is not very helpful in studying domain structure, which has a typical length scale of ~1000 Å and involves millions of atoms, rendering atomic level DFT impractical. Instead, a phase field model [30, 45] simulation tool combining the effects of temperature, strain, and electrostatics, provides the appropriate length scale (~100-1000 Å). Using Landau-Khalatnikov theory, Chen and Li have constructed a phenomenological free energy model for bulk BTO that accurately describes the material phase transitions [28]. We use the finite element implementation of their phase field model [46] to study BTO domain morphologies under mechanical and electrical boundary conditions close to those found in the top region of a Si-integrated BTO film in an EO modulator (see Fig. 1 (b)). And the knowledge of the domain morphology will be used to investigate the Pockels effect.

In this paper, we consider a relatively thick (hundreds of nanometers) BTO film epitaxially integrated in a BTO/STO/Si stack at room temperature that is most relevant for hybrid EO modulators [11-14]. Our simulations focus on the top region near the surface of BTO where the material is fully relaxed and in-plane a-domains dominate at room temperature, as indicated by the red box in Fig. 1 (b). According to [15, 19, 34], approximately 20-30 nm above the BTO/STO interface, BTO begins to transition from c-domain to a-domain orientation, which is the Pockels active region of the BTO film in hybrid devices using such geometry in Refs. [11, 12, 20]. We simulate ~4–10 nm thickness of the surface region and explore the morphology of both polarization and crystallographic structures. We then explore the relations between the polarization and crystallographic structures and Pockels tensor.

II. Methodology

The domain morphology in BTO thin films is controlled by multiple competing mechanisms such as temperature, strain, electrical boundary conditions, film size, etc. that are coupled with each other. To describe the BTO thin film and include these couplings, we construct a three-dimensional free energy model (electrical enthalpy h) [30, 46]:

$$h(u_i, E_i, P_i, P_{i,j}, \theta) = h_{bulk} + h_{wall} + h_{elas} + h_{elec}, (i, j = 1,2,3) \qquad (1)$$

where u_i is the mechanical displacement, E_i electric field, P_i polarization, $P_{i,j} = \partial P_i / \partial x_j$ polarization gradient and θ temperature. h_{bulk} is temperature-dependent bulk free energy of BTO under stress-free conditions in the form of an eighth order Landau-Devonshire polynomial formula [30]. h_{wall} is the domain wall energy associated with the polarization gradient:

$$h_{wall} = \frac{1}{2} G_{ijkl} P_{i,j} P_{k,l}, (i, j, k = 1,2,3), \qquad (2)$$

where G_{ijkl} is the polarization gradient coefficient. h_{elas} is the elastic energy:

$$h_{elas} = \frac{1}{2} c_{ijkl} (\varepsilon_{ij} - \varepsilon_{ij}^0)(\varepsilon_{kl} - \varepsilon_{kl}^0), \qquad (3)$$

where ε_{ij} is strain computed as $\varepsilon_{ij} = \frac{1}{2}(\frac{\partial u_i}{\partial x_j} + \frac{\partial u_j}{\partial x_i})$, c_{ijkl} the elastic stiffness tensor and $\varepsilon_{ij}^0 = Q_{ijkl} P_k P_l$ is the spontaneous strain connected to polarization by the electrostrictive coefficients Q_{ijkl}. h_{elec} is the electrostatic contribution to the electrical enthalpy:

$$h_{elec} = -(\frac{\kappa_o}{2} E_i E_i + E_i P_i), \qquad (4)$$

where κ_o is the permittivity of free space. Details of the free energy model and all the coefficients used in the phase field simulation can be found in Ref. [46].

The evolution of BTO thin film domain morphology is governed by the time-dependent Landau-Khalatnikov equation [30, 47]:

$$\beta \frac{\partial P_i}{\partial t} = -\frac{\delta h}{\delta P_i}, \qquad (5)$$

where β is the kinetic coefficient. Because the time evolution of the free energy is coupled with static partial differential equations of the electrical (Maxwell equations) and mechanical equilibrium states [30, 46], we employ the finite element method and treat the polarization vector $\boldsymbol{P}$, mechanical displacement vector $\boldsymbol{u}$, and electrostatic potential $\boldsymbol{\phi}$ as nodal degrees of freedom (DoFs) and solve for them simultaneously (details of the governing equations in the finite element method can be found in Ref. [46]). We then extract a map of polarization and crystallographic (lattice parameter) domains from the solutions and reveal their relationships.

Here, we will focus on the isothermal condition at 338 K, which is slightly above room temperature (~300 K). Aiming to simulate the ***P4mm*** phase of relaxed BTO near the surface, as reported by Ref. [12, 19, 34], we test a series of temperatures around 300 K under the stress-free boundary condition along the in-plane direction. Based on our simulations as well as the temperature-strain phase diagram reported in Ref. [30], the BTO film is mostly orthorhombic at 300 K, with 338 K being the lowest temperature to stabilize the ***P4mm*** T-phase in relaxed BTO within this model. We generate the initial configuration with unbiased small nodal random fluctuations and let it evolve in accordance with Eq. (5). We want to point out that our simulations are quasi-static. It means the initial configuration is optimized as it converges to the stable equilibrium one, and we focus on that final equilibrium state. Now the essential task is to determine the appropriate electrical and mechanical boundary conditions for the film [48]. The schematic of the simulation cell is shown in Fig. 2. To describe the boundary conditions, we define the center of each plane $\boldsymbol{C_i}$, the normal vector of each plane $\boldsymbol{n_i}$, and the nodal displacement vector from the center $\boldsymbol{r_i}$ (i=1-6). To simulate the large in-plane size of the BTO thin film, we vary the in-plane size from ~20 to 40 nm in order to allow sufficient in-plane space for the evolution of the degrees of freedom and use periodic boundary conditions [48] for polarization $\boldsymbol{P}$: $\boldsymbol{P}(\boldsymbol{C}_i + \boldsymbol{r}_i) = \boldsymbol{P}(\boldsymbol{C}_{\boldsymbol{i+1}} + \boldsymbol{r}_{\boldsymbol{i+1}})$, $(i = 1{,}3)$. We control the strain via displacement in the following form, as $\varepsilon_{ij} = \partial u_i/\partial x_j$,

$$\boldsymbol{u}(\boldsymbol{C}_1 + \boldsymbol{r}_1) = \boldsymbol{u}(\boldsymbol{C}_2 + \boldsymbol{r}_2) + \begin{pmatrix} \varepsilon_x \cdot L \\ 0 \\ 0 \end{pmatrix}, \qquad (6.a)$$

$$\boldsymbol{u}(\boldsymbol{C}_3 + \boldsymbol{r}_3) = \boldsymbol{u}(\boldsymbol{C}_4 + \boldsymbol{r}_4) + \begin{pmatrix} 0 \\ \varepsilon_y \cdot L \\ 0 \end{pmatrix}, \qquad (6.b)$$

where L is the length scale of the simulation cell. This boundary condition creates an average in-plane strain ε_x and ε_y, but allows the out-of-plane direction to respond freely. We emphasize that the zero-strain reference is always the cubic BTO phase even at room temperature. To satisfy the relaxation of strain near the BTO surface [19, 34, 49], as mentioned above, instead of setting $\varepsilon_x = \varepsilon_y = 0$, we assign ε_x and ε_y small tensile strains so as to create an averaged stress-free state in the plane of the film.

To simulate the broken symmetry of the film surface, we apply open-circuit electrical boundary conditions and a pointwise traction-free state for planes centered at $\boldsymbol{C_5}$ and $\boldsymbol{C_6}$ (top and bottom) and let $\boldsymbol{P}$ and $\boldsymbol{u}$ evolve freely. To stabilize the domain morphology with 180-degree domain walls, we use a plane capacitor model, with $\phi(\boldsymbol{C_3}+\boldsymbol{r_3})=0$ as the grounded plane and $\phi(\boldsymbol{C_4}+\boldsymbol{r_4})=const.$, as well as a net charge control technique [46] to stabilize the simulations by placing the external charge at $\boldsymbol{C_4}$ in Fig. 2. If a zero charge is placed at $\boldsymbol{C_4}$, we can maintain $\phi(\boldsymbol{C_4}+\boldsymbol{r_4})=0$ and the average electric field across the film is zero (details of the charge control method are discussed in Ref. [46]). The physical reasoning behind the charge control is rooted in experiment. The external charged particles as well as charged defects cannot be completely avoided that will induce 180-degree domain walls and make the domain morphology more complicated.

III. Crystallographic and polarization distribution results

To extract the domain morphology of the BTO film including possible size effects, we implement isothermal simulations for simulation cells of different sizes. Experimentally, due to the complexity of real boundary conditions, the domain morphologies are quite complicated, with 180-dergee and 90-degree domain walls, etc. [50]. To demonstrate both the polarization and crystallographic distributions in films without 180-degree domain walls, we start our discussion with the phase field simulations that do not use charge control technique mentioned in Sec. II. We vary the in-plane mesh size from 19 × 19 elements, 29 × 29 elements to 39 × 39 elements and fix the out-of-plane dimension at 3 elements. It should be pointed out that there exists a characteristic length scale for each element, defined as $l_0=0.35\sqrt{\frac{G_0P_0}{E_0}}$, where $P_0=0.1811\ C/m^2$ and $E_0=3.21\times10^5\ N/C$ are the spontaneous polarization and coercive field, respectively, derived from the free energy model (Eq. 1) at 398 K. The coercive field is defined as the field needed to trigger 180° domain switching in a monodomain BTO [46]. G_0 is the polarization gradient coefficient defined under the assumption of G_{ijkl} being isotropic. G_0 is related to the domain wall thickness. Hence, the characteristic length scale is determined based on the domain wall thickness. For brevity, the three simulations are referred to as $19l_0\times19l_0\times3l_0$, $29l_0\times29l_0\times3l_0$, and $39l_0\times39l_0\times3l_0$. Based on these assumptions and experimental observations of 90-degree and 180-degree domain walls [51], our simulation volumes correspond approximately to films with dimensions of 20 nm × 20 nm × 4 nm to 40 nm × 40 nm × 4 nm.

The schematic of the simulation cell is shown in Fig. 3(a). To acquire the domain map, we use a plane to scan the nodal values of the various degrees of freedom across the entire cell along the $\boldsymbol{y}$ direction, as indicated by a gray plane in Fig. 3(a). From this, we can extract information on the BTO phase that is encoded piecewise in the degrees of freedom. Fig. 3(b) displays the shear strain ε_{xz} and ε_{yz} of all nodes for three differently sized simulations along with their average values. This shows that the BTO thin film crystallographic structure does not have shear displacement along the ***z*** direction. For each ***x*** position on the two-dimensional scanning plane, we average all degrees of freedom along the ***z*** direction and calculate the standard deviation, represented by the error bar. As will be shown later, the error bars of the ***z*** direction fluctuation can usually be ignored except for transition areas, implying that the thin film degrees of freedom do not have a large variation along the ***z*** direction. This is within our expectations since our simulation covers about 4 nm of thickness and the stable a-domain is ~30 nm thick, as shown in Fig. 1.

An example of such a scan with a plane parallel to the ***x*** and ***z*** axes and located at $y=2l_0$, with size $20l_0 \times 4l_0$ (red line in Fig. 3(a)) in a $20l_0 \times 20l_0 \times 4l_0$ simulation, is displayed in Fig. 3(c). We note that the error bars, representing the ***z*** direction fluctuations of the strain tensor and polarization vector, are very small, which suggests that the simulated segment of the BTO film is uniform along the growth direction. Based on the thermal expansion coefficient of BTO [52, 53], we estimate the lattice constant to be $a_0 = 4.00$ Å at 338 K for the cubic phase. The T-phase strain elements referred to the reference cubic BTO phase are calculated as

$$\varepsilon_a = \frac{a-a_0}{a_0} < 0 \text{ and } \varepsilon_c = \frac{c-a_0}{a_0} > 0, \qquad (7)$$

where a and c represent the short and long axis, respectively. Therefore, we can recover the actual lattice parameter in the simulation cell, which is shown with respect to the right axis in Fig. 3(c). The ε_{zz} is constant and negative in the entire scanning plane, confirming again the in-plane orientation of the a-domain. The majority of ε_{xy} is zero but has a small peak near the crossing point of ε_{xx} and ε_{yy}. The ε_{xx} and ε_{yy} strains fluctuate and have some plateaus within the specific nodal range, which are the BTO domain regions.

To identify these plateaus, we use a plateau searching algorithm to detect the left and right boundary of the plateau. The algorithm uses the criteria between nearest-neighbor nodes that if $|\frac{\varepsilon_i-\varepsilon_{i-1}}{\varepsilon_i}| > t$ and $|\frac{\varepsilon_i-\varepsilon_{i+1}}{\varepsilon_i}| < t$ satisfied (i is the node index), node i is identified as the left boundary of the plateau, where $t = 0.05$ is set to be the tolerance. The criteria indicate a drastic strain change happens to the left of node i, which enters the transition area. Similarly, the right boundary has the criteria $|\frac{\varepsilon_i-\varepsilon_{i-1}}{\varepsilon_i}| < t$ and $|\frac{\varepsilon_i-\varepsilon_{i+1}}{\varepsilon_i}| > t$. Thus, we obtain these plateaus, represented by rectangular boxes in Fig. 3(c). The height of these boxes is set by the standard deviation of the nodal values within each plateau, centered at their mean value, as $(\bar{\varepsilon}_{xx} - \delta\varepsilon_{xx}, \bar{\varepsilon}_{xx} + \delta\varepsilon_{xx})$ or $(\bar{\varepsilon}_{yy} - \delta\varepsilon_{yy}, \bar{\varepsilon}_{yy} + \delta\varepsilon_{yy})$. The T-phase of BTO can be characterized as:

$$\begin{pmatrix} \varepsilon_c & 0 & 0 \\ 0 & \varepsilon_a & 0 \\ 0 & 0 & \varepsilon_{a'} \end{pmatrix} \text{ or } \begin{pmatrix} \varepsilon_a & 0 & 0 \\ 0 & \varepsilon_c & 0 \\ 0 & 0 & \varepsilon_{a'} \end{pmatrix}, \qquad (8)$$

for a-domain along the $\boldsymbol{x}$ and $\boldsymbol{y}$ directions, respectively (here $\varepsilon_c > 0$ and $\varepsilon_{a,a'} < 0$). Theoretically, we should have $\varepsilon_a = \varepsilon_{a'}$, but within the domain characterization process, we allow a finite tolerance:

$$max(|\frac{\varepsilon_a - \varepsilon_{a'}}{\varepsilon_{a'}}|, |\frac{\varepsilon_a - \varepsilon_{a'}}{\varepsilon_a}|) < 0.2. \qquad (9)$$

Using Eq. (8) and (9) to characterize these plateaus, we determine that the plateau ranging from $7l_0$ to $12l_0$ is an a-domain along the $\boldsymbol{x}$ direction and plateaus from $1l_0$ to $2l_0$ and $17l_0$ to $20l_0$ are a-domains along the $\boldsymbol{y}$ direction, meaning that in this scanning plane, the BTO film has a 90-degree domain wall. We also note that the *c/a* ratio is 1.009, agreeing well with the experimental value of 1.011 [54]. The remaining regions in the scanning plane are the transition areas between two T-phase regions. If we zoom in at around $x=6l_0$ and $14l_0$, ε_{xx} and ε_{yy} cross each other and ε_{xy} has a small peak, indicating a non-zero *xy* shear strain. The strain tensor matrix behaves like that of the orthorhombic phase (O-phase), in order to accommodate the rotation of the T-phase axes [40].

We use the same algorithm ($|\frac{P_i - P_{i\pm1}}{P_i}| > t$ or $< t$) to find plateaus of polarization in Fig. 3(d) to obtain information on the polarization variation. The results are also highlighted by rectangular boxes. The polarization variations follow the same pattern as the crystallographic ones, which possesses a 90-degree domain wall. This is within our expectation because, as illustrated in Eq. (3), the strain and polarization are closely coupled. However, by comparing Fig. 3 (c) with (e), we observe that the polarization changes more rapidly than strain across the transition area. If we move the scanning plane in Fig. 3(a) across the entire BTO film and use the same data processing as in Fig. 3(c) and (d), we obtain both the polarization and crystallographic distributions shown in Fig. 4. In the magnified view of the transition area in the bottom panels of Fig. 4 (shown with blue color), we can observe the polarization vectors along $[0\bar{1}0]$ and $[\bar{1}00]$, which belong to P_y and P_x domains, respectively. The size of the simulation cell changes only the size of the domain and the volume fraction of transition area, but not the domain wall thickness. The volume fraction of the transition area for crystallographic distributions is 53%, 34.4% and 20.5% for simulation sizes of $19l_0 \times 19l_0 \times 3l_0$, $29l_0 \times 29l_0 \times 3l_0$, and $39l_0 \times 39l_0 \times 3l_0$, respectively, indicating that this volume fraction decreases as simulation size increases. In general, the transition area with O-phase is significant.

We want to emphasize that the reason why we use the piecewise scanning and averaging first, instead of directly characterizing the domain based on Eq. (8), is that in some complicated boundary condition cases, e.g. with charge control, as will be shown in the following, the fluctuations of polarization and strain are larger than what is shown in Fig. 3 (b)-(e), because of the rather complex domain morphology. Hence, in the main part of the simulation cell, single nodal polarization and strain may not satisfy any domain characterization criteria, but area-averaged values still do. In conclusion, due to the boundary conditions, the whole simulation film is in a-domain. We observe that the crystallographic and polarization variations follow the same pattern (strips along diagonal direction). We also notice that to accommodate the ninety-degree rotation of two regions of T-phase BTO, the domain wall areas experience ***P4mm*** symmetry breaking and behave like pseudo-O-phase. The size effect of simulation cells plays a role in the portion of pseudo-O-phase domain wall area with respect to the whole cells.

We shall now use the same scanning-plane technique and discuss the simulations with charge control and demonstrate how the polarization and crystallographic distributions are affected by 180-degree domain walls induced by charge control. We place the external charge at C_4 in Fig. 2. The simulated BTO film size ranges from $39l_0 \times 19l_0 \times 7l_0$ (size I), $39l_0 \times 29l_0 \times 7l_0$ (size II), $45l_0 \times 45l_0 \times 8l_0$ (size III), and $67l_0 \times 67l_0 \times 13l_0$ (size IV), corresponding to real sizes of ~70 nm × (20-70) nm × 10 nm. Comparing with Fig. 3(b), the ε_{xz} and ε_{yz} fluctuate more rapidly in Fig. 5(a), while the average values are still zero, which confirms again the ignorable z direction shear movement. Fig. 5(b) presents the sample data of the plane at y=$2l_0$ with size $40l_0 \times 8l_0$ in the phase field simulation for size I. We note that the coexistence of positive and negative P_y components is stabilized by the charge control, creating 180-degree domain walls. We can clearly see the larger fluctuation of ε_{xy}, which is non-zero in most nodes, compared with Fig. 3(c). However, as indicated by the magenta boxes $(\bar{\varepsilon}_{xy} - \delta\varepsilon_{xy}, \bar{\varepsilon}_{xy} + \delta\varepsilon_{xy})$ in Fig. 5(b), $\varepsilon_{xy} = 0$ is included, which still satisfies the T-phase zero off-diagonal elements in Eq. (8) on average. Because it is more difficult to satisfy stress-free boundary condition via Eq. (6) in the more complex domain morphologies, we observe that the compressive (negative) strain plateaus of ε_{xx} and ε_{yy} do not overlap with ε_{zz}, unlike in Fig. 3 (c). The large error bar of P_y at $26l_0$ is due to the 180-degree domain wall. To extract the information with larger fluctuations compared with Fig. 3, we increase the tolerance to $t = 0.1$ in the plateau searching algorithm and to 0.65 in domain characterization (Eq. (9)) to address the more complicate domain morphologies. After we scan the entire BTO film, the polarization and crystallographic distributions in Fig. 6 indicate that they have a similar pattern compared with Fig. 4. We still observe ninety-degree domain walls, with the O-phase in the transition area. The relationship of polarization and crystallographic variations is also close to Fig. 4. However, under the effect of charge control, the polarization has a symmetric structure ("V" shape) across the 180-degree domain wall, with opposite P_y vectors in Fig. 6 (a) to (c) top panels. In the region near the 180-degree domain wall (apex of the "V" shape), the crystallographic transition area (shown in blue in Fig. 6) is much larger than that of the 90-degree domain wall. Another possible domain morphology with the coexistence of two head-to-tail polarization channels with opposite directions is shown in Fig. 6(d), a similar structure was reported in Ref. [55, 56]. The simulation cell size does play a role based on Fig. 6 due to the more complex domain morphologies. With larger in-plane dimensions, different domain patterns emerge, e.g. Fig. 6(d). The simulation size also influences the volume fraction of the transition area. The volume fraction of the crystallographic transition area is 48.5% and 39.5% for the size I and size II, respectively. The fraction is 20.9% and 50.9% for size III and IV, respectively. Fig. 7 points out that the 180-degree domain wall is of the Ising type, while the 90-degree domain wall is mixed Ising-Neel type [57] but with smaller magnitude compared with 180-degree domain walls, agreeing well with Ref. [40].

In conclusion, after the introduction of 180-degree domain wall, the 90-degree domain wall observed without charge control holds. The polarization and crystallographic variations also follow the same pattern. The introduction of charge control induces more complex force field in the transition area near “V” shape tip, enlarging the transition area of the crystallographic structure. Also, under the complicate charge control condition, different 180-degree domain wall pattern emerges. This is the net result of the energy optimization of the whole thin film, depending on multiple effects, e.g., the size effect, initial conditions, etc.

IV. Thin film electro-optic response

With the knowledge of domain morphologies, we are ready to explore the Pockels effect of the simulated BTO thin films. The electrical enthalpy h (Eq. (1)) encodes the values of the dielectric tensor with respect to E_i and P_i. We use two approaches to simulate the Pockels effect described in Sec. IV.A and IV.B.. Please note that, due to the specific boundary conditions of the BTO thin film, and the fact that BTO domains all align in-plane, we do not consider simulations with the electric field along the z direction or the z-direction-related dielectric and Pockels tensor.

IV.A Analytical expression for the Pockels tensor

Starting from the definition of the Pockels tensor [58]:

$$r_{ijk} = \frac{\partial}{\partial E_k}(\kappa_0 \kappa_{ij}^{-1}), \tag{10}$$

we can compute the Pockels tensor analytically from the free energy model (details in Supplemental Material Sec. I [59]):

$$r_{ijk}(\varepsilon_{ij}, P_i) = \kappa_0 \varepsilon_{il}^{-1} \beta_{lp}^{-1} \gamma_{pqu} \beta_{qm}^{-1} \beta_{uk}^{-1} \varepsilon_{mj}^{-1} \tag{11}$$

where $\gamma_{ijk} = \frac{\partial^3 h_0}{\partial P_i \partial P_j \partial P_k}$, $\beta_{ij} = \frac{\partial^2 h_0}{\partial P_j \partial P_j}$ and Einstein notation is used. The details of h_0 will be discussed later. In order to distinguish from strain ε, we use κ to represent the dielectric constant. The dielectric tensor of BTO is $\kappa_{ij} = \beta_{ij}^{-1} + \kappa_0 \delta_{ij}$, where β_{ij}^{-1} is actually the susceptibility, κ_0 is the vacuum permittivity and δ_{ij} is Kronecker delta.

The h_0 in Eq. (11) is defined as $h_0 \equiv h_{bulk} + h_{elas}$. Comparing the definition of h_0 with Eq. (1), we ignore h_{wall} because it does not depend on P explicitly and we mainly focus on the pointwise Pockels coefficient calculation with the analytical form (Eq. (11)). A few words need to be said about h_{elas} in h_0. Based on the analysis in Refs. [60-63], the Pockels coefficient includes the ionic and piezoelectric contributions. If the BTO lattice vectors stay constant, then there will be no piezoelectric contribution, which is the so-called "clamped" Pockels tensor. If the BTO lattice vectors change is allowed (through the converse piezoelectric effect), the piezoelectric contribution is nonzero, which is the so-called "unclamped" case. In order to include the converse piezoelectric effect, we need to minimize h_0 with respect to strain ε_{ij} ($\partial h_0/\partial \varepsilon_{ij} = 0$). Based on Eq. (1) and (3), we obtain the following stress condition:

$$\sigma_{ij} = \frac{\partial h}{\partial \varepsilon_{ij}} = \frac{\partial h_{elas}}{\partial \varepsilon_{ij}} = c_{ijkl}(\varepsilon_{kl} - \varepsilon_{kl}^0) = 0, \tag{12}$$

where σ_{ij} is stress tensor. Eq. (12) illustrates the reason why some researchers use the terminology stress-free Pockels tensor as "unclamped" Pockels tensor [60]. Eq. (12) also shows that due to the stress-free condition, the elastic energy is zero and the BTO lattice vectors are allowed to change. Consequently, in our calculations, if we set $h_0 = h_{bulk}$ ($h_{elas} = 0$), we include the converse piezoelectric response and the Pockels coefficients include both ionic and piezoelectric contributions. Alternatively, if we use $h_0 = h_{bulk} + h_{elas}$, and fix the strain ε_{ij} value in Eq. (3) determined by the strain from domain morphology calculations, the Pockels tensor corresponds to clamped conditions. Nonzero h_{elas} term means that the stress-free condition is not satisfied (Eq. (12)). And the fixed strain means no change of the lattice vectors. Based on Refs. [62, 63], the unclamped Pockels coefficients are approximately double of the clamped coefficients. As will be shown later, in our simulations, h_{elas} has negative contribution to the value of Pockels coefficients, in agreement with Refs [62, 63].

To obtain the Pockels tensor morphology for the entire BTO thin film, we use Eq. (11) to calculate the nodal Pockels tensor, where ε_{ij} and P_i are the nodal values from the domain morphology calculations. As a demonstration of Eq. (11), we calculate an unclamped Pockels tensor with the bulk ***P4mm*** BTO polarization value of $P = (0,0,0.24)\ C/m^2$ under the simulation temperature (338 K) and get $r_{13} = 17.44\ pm/V$, $r_{33} = 264.35\ pm/V$ and $r_{42} = 139.99\ pm/V$, compared with experimental values $r_{13} = 19.5\ pm/V$, $r_{33} = 97\ pm/V$ and $r_{42} = 1300\ pm/V$ [21, 58, 64, 65]. Taking the temperature dependence of the Pockels tensor [62] into consideration, our r_{13} and r_{33} agree well with first principles predictions under the simulation temperature but r_{42} is underestimated significantly, which will be discussed later.

We will use the domain morphology results from Fig. 4 and Fig. 6 to calculate the Pockels coefficient (r_{13}, r_{33} and r_{42}) morphologies in thin films and the results are displayed in

Fig. 8 and Fig. 9, corresponding to unclamped and clamped conditions, respectively. For simplicity, we only plot results for three simulation cell sizes because the rests are similar. In Fig. 8, 9 (a) and (d) panels, we only simulate the electric field along the y direction because the x and y directions are equivalent in these cases. For Fig. 8, 9 (b) and (c) panels, because we have charge control conditions along the y direction, we simulate the electric field along both the x and y directions. It is worth mentioning the notation used for the Pockels tensor. Compared with bulk BTO, BTO thin films with multidomain structure have different orientations of the long axis in different regions. Hence, instead of simply using r_{42}, r_{33} and r_{13} defined in bulk BTO, the accurate notation should be r_{yxy} (r_{xyx}), r_{yyy} (r_{xxx}) and r_{xxy} (r_{yyx}), depending on the direction of the applied electric field, indicated in Fig. 8 and 9. We find that the Pockels coefficient distributions agree well with crystallographic and polarization distributions, as we can clearly distinguish the domain wall area and bulk-like region. The values of r_{yxy} (r_{xyx}) and r_{yyy} (r_{xxx}) in the bulk-like region agree well with our bulk ***P4mm*** BTO results, while the values of r_{xxy} (r_{yyx}) do not. We attribute this to the fact that the variation of the Pockels coefficient is larger than its magnitude ($r_{13} = 17.44\, pm/V$). We also notice that the Pockels coefficients in the domain wall area fluctuate significantly and are higher than those in the bulk-like region on average in Fig. 8 and Fig. 9. Furthermore, based on Fig. 4 and 6, BTO thin films have *a1/a2* domain, corresponding to long axis along the *x/y* direction respectively. For a specific Pockels tensor element (e.g. r_{yxy}), applying the electric field along either the x or the y direction only activates half of the thin film Pockels response, while the other half remains inactive (zero Pockels coefficient). This phenomenon is shown in Fig. 8 and 9. Comparing Fig. 8 and Fig. 9, we observe that the unclamped Pockels coefficients are approximately twice larger than those under the clamped condition, which agrees qualitatively with the experimental and DFT results [63-65].

IV.B Numerical fitting of the effective Pockels tensor for the entire thin film

The approach in Sec. IV.A is analytical and does not require applying the actual electric field in the simulations. The Pockels coefficients are the local nodal values. We believe an alternative approach to simulate the experimental measurement and obtain the average Pockels coefficients of the entire film is insightful. As a complement to Sec. IV.A, the average scheme models the actual response of the BTO film to the electric field and includes all possible crystal and polarization changes.

We consider the simulation cell from Fig. 4 (b) (no charge control conditions) as a demonstration. In this configuration, because the x and y directions are equivalent, we only test the case with the electric field E_y along the y direction. To simulate the Pockels effect, a fine grid is needed in order to capture the polarization variation as the film responds to the external electric field. Consider for example, the simulation shown Fig. 4 (b); we double and quadruple the original mesh grid (29 × 29 × 3 elements) to 58 ×58 × 6 elements and

116 × 116 × 12 elements, respectively (the schematic is shown in Fig. 10 (a)). As shown in Fig. 10 (a), because we are simulating the same film volume, the characteristic length is decreased by half and quarter accordingly and the total volume is kept the same. It is different from what is shown in Fig. 4 (c) that simulates a larger volume of BTO than that in Fig. 4 (b). Details of the mesh size convergence test can be found in the Supplemental Material Sec. II [59]. In conclusion, the domain morphology is not very sensitive to the fineness of the mesh grid, while the Pockels coefficients are very sensitive to it. The values of the Pockels coefficients change significantly from the 29×29×3-element mesh to 58×58×6-element one but converge for the finer mesh. Thus, we believe that the 58×58×6-elements grid is sufficient to capture the Pockels response of the BTO film shown in Fig. 4 (b). The simulation result for the 58×58×6-element mesh is shown in Fig. 10. The metal contact is placed along the y direction. A small probe electric field E_{probe} is added to the E_y. The probe field can induce the polarization vector change, and the dielectric tensor ε_{xx}, ε_{xy} and ε_{yy} can then be obtained based on the change of polarization. In experiments [12, 19], similar setup is used to measure the effective Pockels coefficient. Figs. 10 (c)-(e) display the computed inverse of the dielectric tensor under different values of the external electric field E_y. Based on Eq. (10), we use the linear fitting, and the slopes are the Pockels tensor elements. From our results, the effective r_{xxy} and r_{yyy}, corresponding to r_{13} and r_{33} in bulk BTO, respectively, and are approximately a half of the bulk values. The effective r_{yxy}, corresponding to r_{42} in bulk BTO, is still underestimated compared to the experimental and theoretical results, and is also smaller than the analytical value in our model. Intuitively, for a specific Pockels tensor element (e.g. r_{yyy}) and under a specific direction of electric field, only half of the local Pockels element is nonzero, based on Figs. 8 and 9. Consequently, the average Pockels coefficient is a half of the bulk value. However, based on our results, not all the components are reduced by a factor of two. We believe that the domain wall has a significant contribution to the average Pockels tensor. And the impact of the domain wall on the Pockels tensor depends on which Pockels component we consider.

We also apply the electric field and calculate the average polarization change for the cases with charge control conditions (Fig. 6). However, we notice the strong negative capacitance effect [66, 67] along with the 180-degree domain wall movement. This result needs more consideration and is beyond the scope of this paper. Consequently, we include our observation in the Supplemental Material [59] (Sec. III) but do not include the Pockels calculation for these boundary conditions.

IV.C Discussion of the thin film electro-optic response

It is worth discussing that whether the large external electric field may influence the BTO thin film domain morphology and induce the domain wall movement. If the domain wall moves significantly or the whole film evolves to a monodomain structure after we applied the external electric field, then our analysis in Sec. IV.A is somewhat problematic. Here, we mainly focus on the BTO thin film epitaxially constrained by the Si substrate. The domain wall can be pinned by strain from the substrate. To address this question, we analyze the domain wall position and confirm that the domain wall movement is ignorable compared with the simulation scale, even under quite a large critical electric field. Details are included in the Supplemental Material [59] (Sec. IV). This phenomenon was also studied experimentally by Nordlander et al. [31], who came to a similar conclusion.

After we map the Pockels tensor across the films, there are still several questions left to be discussed. Firstly, to correct the substantial underestimation of r_{42}, we believe that some modifications to the free energy model are necessary. The original free energy model coefficients are used to describe BTO phase transition and fitted based on the polarization and crystallographic phase of BTO and double well energy profile from experiments and first principles calculations, excluding the EO data. The Pockels effect is a nonlinear optical effect, which requires a very accurate free energy model and any small inaccuracy in the BTO free energy model can induce significant errors. To illustrate this point, we test the free energy model [68] (details of this free energy model test calculations are included in the Supplemental Materials Sec. V [59]), whose coefficients of h_{bulk} polynomial and the strain polarization coupling term (elastic energy h_{elas}) are slightly different with the model [30] used in our phase field simulations in previous sections. As shown in the Supplemental Material Sec. V [59], appropriate tunning of free energy model formalism and coefficients can yield better Pockels coefficient value (unclamped r_{42} increased to ~1300 pm/V, agreeing well with experimental value), while the crystallographic and polarization properties stay the same. Secondly, more research on the Pockels tensor in the domain wall area needs to be done. Based on our results, the domain wall area behaves as a pseudo-O-phase for polarization and crystallographic structure. Additionally, the impact of the domain wall on the average Pockels coefficient is anisotropic and depends on the component of the Pockels tensor. In reality, the BTO domain wall is anisotropic and may contain defects, which makes it more complicated than the simplified description in our model (Eq. (2)).

V. Conclusions

Using a finite element implementation of the phase field model, we simulated the near-surface portion of a BTO thin film integrated on an STO/Si substrate, as used in hybrid EO modulators. Our simulation results show a mosaic of orthogonal a-oriented domains with only an in-plane component of polarization, in agreement with the experimental observations [12, 34, 49]. We study the domain morphologies of BTO thin films and analyze the polar and crystallographic structure variation. Despite the film being in the tetragonal phase, a quasi-orthorhombic phase is found in the transition regions between domains of different orientation. Then using the established domain morphology, we simulate the Pockels effect and find that the Pockels coefficient morphology of the film follows the same pattern as the crystallographic and polarization distributions. As pointed out in the introduction, the strength of the EO modulation is quantified by the effective Pockels coefficient. With the electric field applied in-plane along either the *x* or *y* directions, a specific Pockels tensor element is only active in a part of the film. Our results suggest that the effective Pockels coefficient of Si-integrated BTO films used in EO modulators may be sensitive to the details of the domain morphology as well as to the domain wall distribution. And the impact of domain wall on the effective Pockels effect is anisotropic. The reduction of the effective Pockels coefficient, observed experimentally in thin films, is probably caused by the complex domain morphology, existence of the domain walls and possibly by the c- to a-domain transition with the film thickness. We believe that the details of the relationship between the polarization and crystallographic variations, and the Pockels effect in thin films can provide guidance for further optimization these devices.

Acknowledgements

We thank Agham Posadas for insightful discussion and critical reading of the manuscript. The work is supported by the Air Force Office of Scientific Research under grant FA9550-18-1-0053.

References

[1] G. T. Reed, G. Mashanovich, F. Y. Gardes and D. J. Thomson, "Silicon optical modulators," Nat. Photon. **4**, 518 (2010).

[2] M. J. R. Heck, H.-W. Chen, A. W. Fang, B. R. Koch, D. Liang, H. Park, M. N. Sysak and J. E. Bowers, "Hybrid Silicon Photonics for Optical Interconnects," IEEE J. Sel. Top. Quantum Electron. **17**, 2 (2011).

[3] K. Vandoorne, P. Mechet, T. Van Vaerenbergh, M. Fiers, G. Morthier, D. Verstraeten, B. Schrauwen, J. Dambre and P. Bienstman, "Experimental demonstration of reservoir computing on a silicon photonics chip," Nat. Commun. **5**, 3541 (2014).

[4] A. A. Demkov, C. Bajaj, J. G. Ekerdt, C. J. Palmström, and S. J. Ben Yoo, “Materials for emergent silicon-integrated optical computing,” J. Appl. Phys. **130**, 070907 (2021).

[5] J. Feldmann, N. Youngblood, C. D. Wright, H. Bhaskaran and W. H. P. Pernice, "All-optical spiking neurosynaptic networks with self-learning capabilities," Nature **569**, 208–214 (2019).

[6] Q. Zhang, H. Yu, M. Barbiero, B. Wang and M. Gu, "Artificial neural networks enabled by nanophotonics," Light Sci. Appl. **8**, 42 (2019).

[7] H. Tan, Z. Ni, W. Peng, S. Du, X. Liu, S. Zhao, W. Li, Z. Ye, M. Xu, Y. Xu, X. Pi, D. Yang, "Broadband optoelectronic synaptic devices based on silicon nanocrystals for neuromorphic computing," Nano Energy **52**, 422-430 (2018).

[8] F. Flamini, N. Spagnolo and F. Sciarrino, "Photonic quantum information processing: a review," Rep. Prog. Phys. **82**, 016001 (2019).

[9] X. Qiang, X. Zhou, J. Wang, C. M. Wilkes, T. Loke, S. O'Gara,L. Kling, G. D. Marshall, R. Santagati, T C. Ralph, J. B. Wang, J. L. O'Brien, M. G. Thompson and J. C. F. Matthews, "Large-scale silicon quantum photonics implementing arbitrary two-qubit processing," Nat. Photon. **12**, 534–539 (2018).

[10] A. Rahim, A. Hermans, B. Wohlfeil, D. Petousi, B. Kuyken, D. Van Thourhout and R. Baetsa, "Taking silicon photonics modulators to a higher performance level: state-of-the-art and a review of new technologies," Adv. Photonics **3**, 024003 (2021).

[11] F. Eltes, G. E. Villarreal-Garcia, D. Caimi, H. Siegwart, A. A. Gentile, A. Hart, P. Stark, G. D. Marshall, M. G. Thompson, J. Barreto, J. Fompeyrine and S. Abel, "An integrated optical modulator operating at cryogenic temperatures," Nat. Mater. **19**, 1164–1168 (2020).

[12] S. Abel, F. Eltes, J. E. Ortmann, A. Messner, P. Castera, T. Wagner, D. Urbonas, A. Rosa, A. M. Gutierrez, D. Tulli, P. Ma, B. Baeuerle, A. Josten, W. Heni, D. Caimi, L. Czornomaz, A. A. Demkov, J. Leuthold, P. Sanchis and J. Fompeyrine, "Large Pockels effect in micro- and nanostructured barium titanate integrated on silicon," Nat. Mater. **18**, 42 (2019).

[13] W. H. P. Pernice, C. Xiong, F. J. Walker and H. X. Tang, "Design of a Silicon Integrated Electro-Optic Modulator Using Ferroelectric $BaTiO_3$ Films," IEEE Photon. Technol. Lett. **26**, 13 (2014).

[14] C. Xiong, W. H. P. Pernice, J. H. Ngai, J. W. Reiner, D. Kumah, F. J. Walker, C. H. Ahn, and H. X. Tang, "Active Silicon Integrated Nanophotonics: Ferroelectric $BaTiO_3$ Devices," Nano Lett. **14**, 3 (2014).

[15] A. B. Posadas, H. Park, M. Reynaud, W. Cao, J. D. Reynolds, W. Guo, V. Jeyaselvan, I. Beskin, G. Mashanovich, J. H. Warner, and A. A. Demkov, "Thick $BaTiO_3$ epitaxial films integrated on Si by RF sputtering for electro-optic modulators in Si photonics," ACS Appl. Mater. Interfaces **13**, 51230 (2021).

[16] C. Wang, M. Zhang, X. Chen, M. Bertrand, A. Shams-Ansari, S. Chandrasekhar, P. Winzer and M. Lončar, "Integrated lithium niobate electro-optic modulators operating at CMOS-compatible voltages," Nature **562**, 101 (2018).

[17] J. Leuthold, C Koos, W. Freude, L. Alloatti, R. Palmer, D. Korn, J. Pfeifle, M. Lauermann, R. Dinu, S. Wehrli, M. Jazbinsek, P. Gunter, M. Waldow, T. Wahlbrink, J. Bolten, H. Kurz, M. Fournier, J.-M. Fedeli, H. Yu, and W. Bogaerts, "Silicon-Organic Hybrid Electro-Optical Devices," IEEE J. Sel. Topics Quantum Electron. **19**, 6 (2013).

[18] W. Heni, Y. Kutuvantavida, C. Haffner, H. Zwickel, C. Kieninger, S. Wolf, M. Lauermann, Y. Fedoryshyn, A. F. Tillack, L. E. Johnson, D. L. Elder, B. H. Robinson, W. Freude, C. Koos, J. Leuthold, and L. R. Dalton, "Silicon−Organic and Plasmonic−Organic Hybrid Photonics," ACS Photonics **4**, 7 (2017).

[19] S. Abel, T. Stöferle, C. Marchiori, D. Caimi, L. Czornomaz, M. Stuckelberger, M. Sousa, B. J. Offrein, and J. Fompeyrine, "A Hybrid Barium Titanate–Silicon Photonics Platform for Ultraefficient Electro-Optic Tuning," J. Light. Technol. **34**, 8 (2016).

[20] W. Guo, A. B. Posadas, and A. A. Demkov, "Epitaxial integration of $BaTiO_3$ on Si for electro-optic applications, " J. Vac. Science & Technology A **39**, 030804 (2021).

[21] A. Yariv, and P. Yeh, Optical Waves in Crystals (John Wiley & Sons, 1984).

[22] E. L. Wooten, K. M. Kissa, A. Yi-Yan, E. J. Murphy, D. A. Lafaw, P. F. Hallemeier, D. Maack, D. V. Attanasio, D. J. Fritz, G. J. McBrien, and D. E. Bossi, "A review of lithium niobate modulators for fiber-optic communications systems," IEEE J. Sel. Topics Quantum Electron. **6**, 1 (2000).

[23] B. Chmielak, M. Waldow, C. Matheisen, C. Ripperda, J. Bolten, T. Wahlbrink, M. Nagel, F. Merget and H. Kurz, "Pockels effect based fully integrated, strained silicon electro-optic modulator," Opt. Express **19**, 17212–17219 (2011).

[24] B. Desiatov and M. Lončar, "Silicon photodetector for integrated lithium niobate photonics," Appl. Phys. Lett. **115**, 121108 (2019).

[25] R. A. McKee, F. J. Walker, and M. F. Chisholm, "Crystalline Oxides on Silicon: The First Five Monolayers," Phys. Rev. Lett. **81**, 3014 (1998).

[26] A. A. Demkov and A.B. Posadas, Integration of Functional Oxides with Semiconductors, (Springer, 2014).

[27] Y. Wei, X. Hu, Y. Liang, D. C. Jordan, B. Craigo, R. Droopad, Z. Yu, A. Demkov, J. L. Edwards, Jr., and W. J. Ooms, "Mechanism of cleaning Si (100) surface using Sr or SrO for the growth of crystalline $SrTiO_3$ films," J. of Vac. Sci. & Technol. B **20**, 1402 (2002)

[28] Y. L. Li, L. E. Cross and L. Q. Chen, "A phenomenological thermodynamic potential for single crystals," J. Appl. Phys. **98**, 064101 (2005).

[29] B. Wagué, J.-.B. Brubach, G. Niu, G. Dong, L. Dai, P. Roy, G. Saint-Girons, P. Rojo-Romeo, Y. Robach, "Structural studies of epitaxial $BaTiO_3$ thin film on silicon," Thin Solid Films **693**, 137636 (2020).

[30] Y. L. Li and L. Q. Chen, "Temperature-strain phase diagram for thin films," Appl. Phys. Lett. **88**, 072905 (2006).

[31] J. Nordlander, F. Eltes, M. Reynaud, J. Nürnberg, G. De Luca, D. Caimi, A. A. Demkov, S. Abel, M. Fiebig, J. Fompeyrine, and M. Trassin, "Ferroelectric domain architecture and poling of $BaTiO_3$ on Si," Phys. Rev. Materials **4**, 034406 (2020).

[32] R. Ahluwalia, T. Lookman, A. Saxena, and W. Cao, "Domain-size dependence of piezoelectric properties of ferroelectrics," Phys. Rev. B **72**, 014112 (2005).

[33] N. Floquet and C. Valot, "Ferroelectric domain walls in $BaTiO_3$: Structural wall model interpreting fingerprints in XRPD diagrams," Ferroelectrics **234**, 107-122 (1999).

[34] C. Dubourdieu, J. Bruley, T. M. Arruda, A. Posadas, J. Jordan-Sweet, M. M. Frank, E. Cartier, D. J. Frank, S. V. Kalinin, A. A. Demkov, and V. Narayanan, "Switching of ferroelectric polarization in epitaxial $BaTiO_3$ films on silicon without a conducting bottom electrode," Nat. Nanotechnol. **8**, 748–754 (2013).

[35] Y. Cho, P. Ponath, L. Zheng, B. Hatanpaa, K. Lai, A. A. Demkov, and M. C. Downer, "Polarization retention in ultra-thin barium titanate films on Ge(001)," Appl. Phys. Lett. **112**, 162901 (2018).

[36] K. J. Kormondy, Y. Cho, A. B. Posadas, L. Zheng, K. Lai, Q. Wang, M. J. Kim, Q. He, A. Y. Borisevich, M. C. Downer, and A. A. Demkov, "Piezoelectric modulation of nonlinear optical response in $BaTiO_3$ thin film," Appl. Phys. Lett. **113**, 132902 (2018).

[37] P. Ponath, K. Fredrickson, A. B. Posadas, Y. Ren, X. Wu, R. K. Vasudevan, M. B. Okatan, S. Jesse, T. Aoki, M. R. McCartney, D. J. Smith, S. V. Kalinin, K. Lai and A. A. Demkov, "Carrier density modulation in a germanium heterostructure by ferroelectric switching," Nat. Commun. **6**, 6067 (2015).

[38] C.-L. Jia, S.-B. Mi, K. Urban, I. Vrejoiu, M. Alexe and D. Hesse, "Atomic-scale study of electric dipoles near charged and uncharged domain walls in ferroelectric films," Nat. Mater. **7**, 57 (2008).

[39] S. Li, Y. L. Zhu, Y. L. Tang, Y. Liu, S. R. Zhang, Y. J. Wang, and X. L. Ma, "Thickness-dependent a_1/a_2 domain evolution in ferroelectric $PbTiO_3$ films," Acta Mater. **131**, 123 (2017).

[40] W. Cao and L. E. Cross, "Theory of tetragonal twin structures in ferroelectric perovskites with a first-order phase transition," Phys. Rev. B **44**, 5 (1991).

[41] S. Tinte, M. G. Stachiotti, M. Sepliarsky, R. L. Migoni and C. O. Rodriguez, "Atomistic modelling of $BaTiO_3$ based on first-principles calculations," J. Phys.: Condens. Matter **11**, 9679 (1999).

[42] K. D. Fredrickson and A. A. Demkov, "Switchable conductivity at the ferroelectric interface: Nonpolar oxides," Phys. Rev. B **91**, 115126 (2015).

[43] R. I. Eglitis and D. Vanderbilt, "Ab initio calculations of $BaTiO_3$ and $PbTiO_3$ (001) and (011) surface structures," Phys. Rev. B **76**, 155439 (2007).

[44] R.I. Eglitis, J. Kleperis, J. Purans, A.I. Popov and R. Jia, "Ab initio calculations of $CaZrO_3$ (011) surfaces: systematic trends in polar (011) surface calculations of ABO_3 perovskites," J. Mater. Sci. **55**, 203-217 (2020).

[45] J.-J. Wang, B. Wang, and L.-Q. Chen, "Understanding, Predicting, and Designing Ferroelectric Domain Structures and Switching Guided by the Phase-Field Method," Annu. Rev. Mater. Res. **49**, 127–52 (2019).

[46] A. Y. Woldman and C. M. Landis, "Thermo-electro-mechanical phase-field modeling of paraelectric to ferroelectric transitions," Int. J. Solids Struct. **178-179**, 19-35 (2019).

[47] L. D. Landau and I. M. Khalatnikov, "On the anomalous absorption of sound near a second-order phase transition point," Dok. Akad. Nauk SSSR **96**, 469–472 (1954).

[48] I. Muench, A. R. Balakrishna, and J. E. Huber, "Periodic boundary conditions for the simulation of 3D domain patterns in tetragonal ferroelectric material," Arch. Appl. Mech. **89**, 955–972 (2019).

[49] S. Abel, T. Stöferle, C. Marchiori, C. Rossel, M. D. Rossell, R. Erni, D. Caimi, M. Sousa, A. Chelnokov, B. J. Offrein and J. Fompeyrine, "A strong electro-optically active lead-free ferroelectric integrated on silicon," Nat. Commun. **4**, 1671 (2013).

[50] A. R. Balakrishna, J. E. Huber, and I. Munch, "Nanoscale periodic domain patterns in tetragonal ferroelectrics: A phase-field study," Phys. Rev. B **93**, 174120 (2016).

[51] G. Catalan, J. Seidel, R. Ramesh, and J. F. Scott, "Domain wall nanoelectronics," Rev. Mod. Phys. **84**, 119 (2012).

[52] R. G. Rhodes, "Barium titanate twinning at low temperatures, "Acta Cryst. **4**, 2 (1951).

[53] J. A. Bland, "The thermal expansion of cubic barium titanate ($BaTiO_3$) from 350° C to 1050° C," Can. J. Phys. **37**, 417 (1959).

[54] M. El Marssi, F. Le Marrec, I. A. Lukyanchuk, and M. G. Karkut, "Ferroelectric transition in an epitaxial barium titanate thin film: Raman spectroscopy and x-ray diffraction study," J. of Appl. Phys. **94**, 3307 (2003).

[55] J. Hlinka, and P. Marton, "Ferroelastic Domain Walls in Barium Titanate-Quantitative Phenomenological Model," Integr. Ferroelectr. **101**, 50-62 (2010).

[56] P. Marton, and J. Hlinka, "Simulation of domain patterns in $BaTiO_3$, " Phase Transit. **79**, 6-7 (2006).

[57] D. Lee, R. K. Behera, P. Wu, H. Xu, Y. L. Li, S. B. Sinnott, S. R. Phillpot, L. Q. Chen, and V. Gopalan, "Mixed Bloch-Néel-Ising character of 180° ferroelectric domain walls," Phys. Rev. B **80**, 060102(R) (2009).

[58] R. W. Boyd, Nonlinear Optics, 3rd ed. (Elsevier, San Diego, 2008).

[59] See Supplemental Material at [URL will be inserted by publisher] for details of equation derivations as well as extra discussions to support the conclusions in this paper.

[60] A. K. Hamze, M. Reynaud, J. Geler-Kremer, and A. A. Demkov, “Design rules for strong electro-optic materials,” Npj Comput. Mater. **6**, 130 (2020).

[61] T. Paoletta and A. A. Demkov, “Pockels effect in low-temperature rhombohedral $BaTiO_3$,” Phys. Rev. B **103**, 014303 (2021).

[62] M. Veithen and Ph. Ghosez, "Temperature dependence of the electro-optic tensor and refractive indices of $BaTiO_3$ from first principles," Phys. Rev. B **71**, 132101 (2005).

[63] I. Kim, T. Paoletta and A. A. Demkov, "An Ab-Initio Study of the Pockels Effect in Tetragonal $BaTiO_3$," (Under review).

[64] M. Zgonik, P. Bernasconi, M. Duelli, R. Schlesser, P. Günter, M. H. Garret, D. Rytz, Y. Zhu, and X. Wu, "Dielectric, elastic, piezoelectric, electro-optic, and elasto-optic tensors of $BaTiO_3$ crystals," Phys. Rev. B **50**, 5941 (1994).

[65] A. Karvounis, F. Timpu, V. V. Vogler-Neuling, R. Savo, and R. Grange, "Barium Titanate Nanostructures and Thin Films for Photonics," Adv. Opt. Mater. **8**, 24 (2020).

[66] A. I. Khan, K. Chatterjee, B. Wang, S. Drapcho, L. You, C. Serrao, S. R. Bakaul, R. Ramesh and S. Salahuddin, "Negative capacitance in a ferroelectric capacitor," Nat. Mater. **14**, 182 (2015).

[67] J. Íñiguez, P. Zubko, I. Luk'yanchuk and A. Cano, "Ferroelectric negative capacitance," Nat. Rev. Mater. **4**, 243 (2019).

[68] Y. Su and C. M. Landis, "Continuum thermodynamics of ferroelectric domain evolution: Theory, finite element implementation, and application to domain wall pinning," J. Mech. Phys. Solids **55**, 280 (2007).

Figures

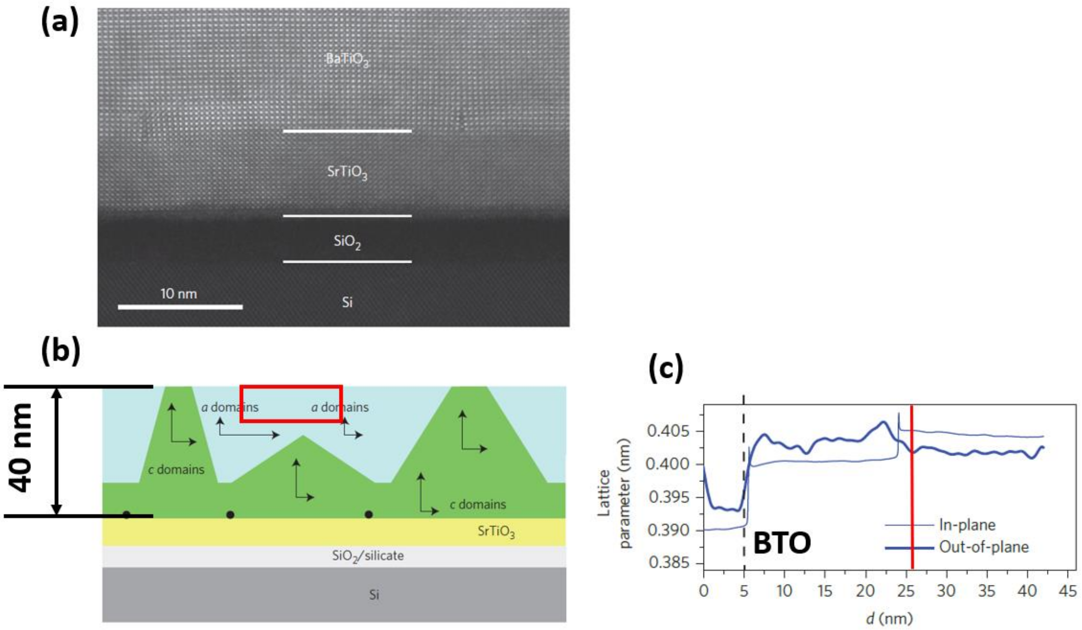

Fig. 1 (a) STEM image of BTO/STO/SiO_2/Si stack. (b) Schematic representation of the domain structure of the heterostructure. (c) Lattice parameter profiles as a function of the distance *d*

from the interface between the amorphous interfacial layer and the crystalline STO layer. It is calculated by averaging data of a specific area of the BTO film. The red line separates the c-domain region to the left and a-domain region to the right. (a)-(c) are from Ref. [34].

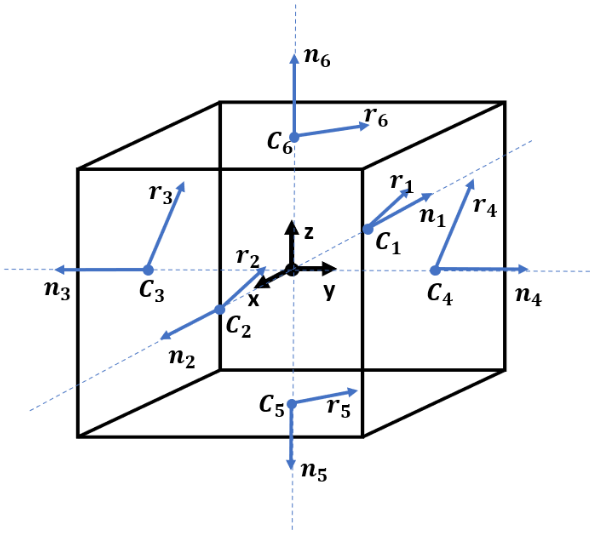

Fig. 2 Finite element method simulation cell. $\boldsymbol{C}_i$ is the center of each plane (i=1-6). $\boldsymbol{n}_i$ is the normal vector of each plane. $\boldsymbol{r}_i$ is the displacement vector of each node on plane i, where $\boldsymbol{r}_1 = \boldsymbol{r}_2 = (0, y, z), \boldsymbol{r}_3 = \boldsymbol{r}_4 = (x, 0, z)$ and $\boldsymbol{r}_5 = \boldsymbol{r}_6 = (x, y, 0)$. Every nodal coordinate on plane i can be represented as $\boldsymbol{x} = \boldsymbol{C}_i + \boldsymbol{r}_i$.

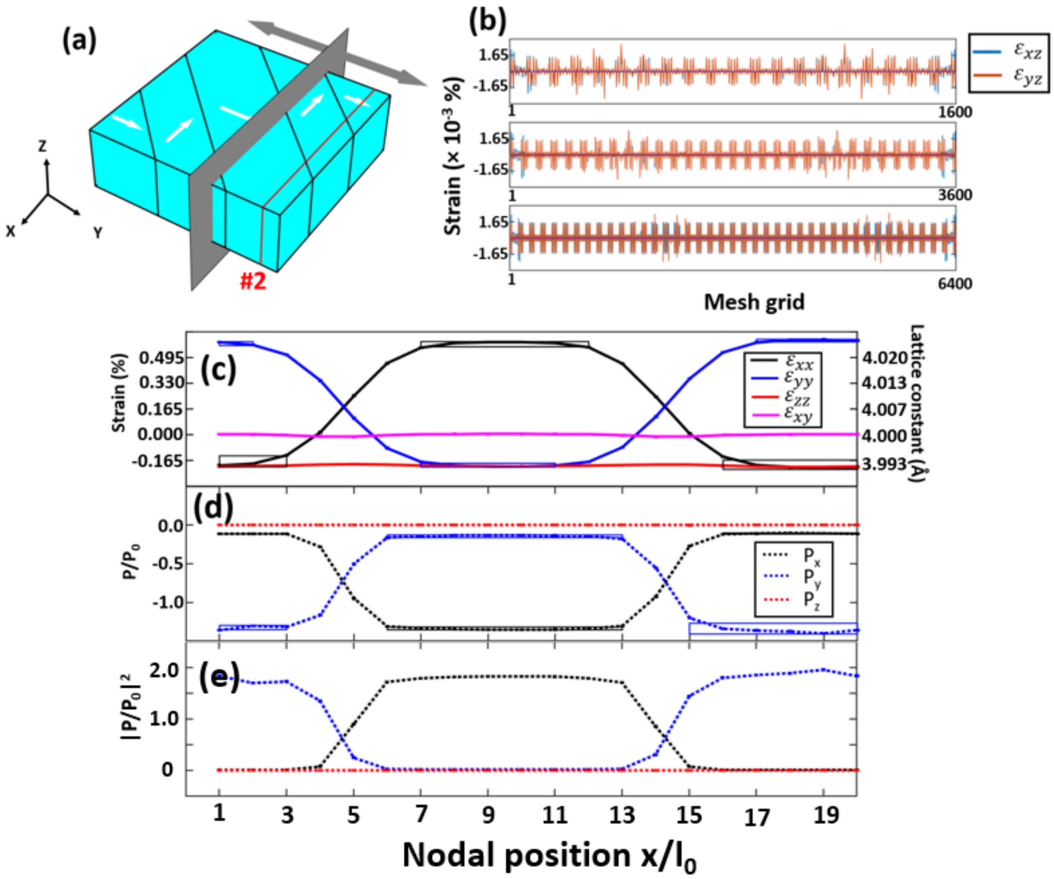

Fig. 3 (a) Schematic picture of the simulation cell. Each sub-region with a white arrow represents an a-domain of BTO and its polarization direction. Note that the specific domain structure is only for demonstration and is not the actual domain morphology. The gray plane is the virtual data scanning plane, which can be moved along the directions of the gray arrows. The red line is the second grid plane in the cell, which is used to demonstrate the sample data scanning process. (b) The values of shear strain ε_{xz} and ε_{yz} of all nodes in 20 × 20 × 4 (1600 nodes), 30 × 30 × 4 (3600 nodes), and 40 × 40 × 4 (6400 nodes) simulation sizes, respectively. The average values of the whole cell are $\varepsilon_{xz} = \varepsilon_{zx} = 0.0$ and $\varepsilon_{yz} = \varepsilon_{zy} = 0.0$ for all three sizes. (c) Data for strain tensor elements, (d) polarization vectors and (e) polarization magnitude square of the second grid plane in the 20 × 20 × 4 simulation. The lattice constant values are calculated based on the strain tensor. The virtual scanning plane size is $20l_0$ along x and $4l_0$ along z. We plot the data along the x direction, while the z direction variation is depicted by the error bar. $P_0 = 0.1811\ C/m^2$ is the spontaneous polarization that is used to normalize the polarization vector. In panel (e), we plot polarization square for better clarification because based on the definition of spontaneous strain, $\varepsilon \propto |P|^2$.

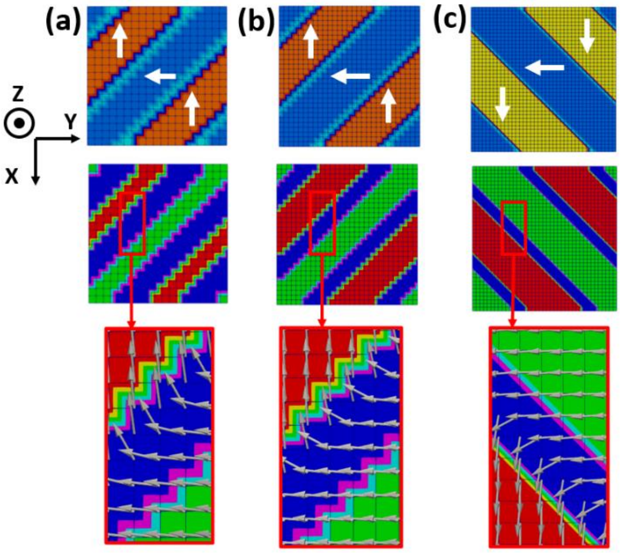

Fig. 4 20l_0 × 20l_0 × 4l_0 , 30l_0 × 30l_0 × 4l_0, and 40l_0 × 40l_0 × 4l_0 phase field simulations in (a), (b), and (c), respectively. The top row of panels of (a) to (c) are polarization ~~domain~~ structures, where dark blue regions are P_y domains, orange and yellow are P_x domains, and cyan is the transition area. The polarization directions are depicted by white arrows. The middle row of panels is crystallographic ~~domain~~ structure, where red and green are a-domains along x and y directions, respectively, and blue represents the transition area. The bottom row of panels is the magnification of the red boxes in the middle row, where white arrows represent polarization vectors.

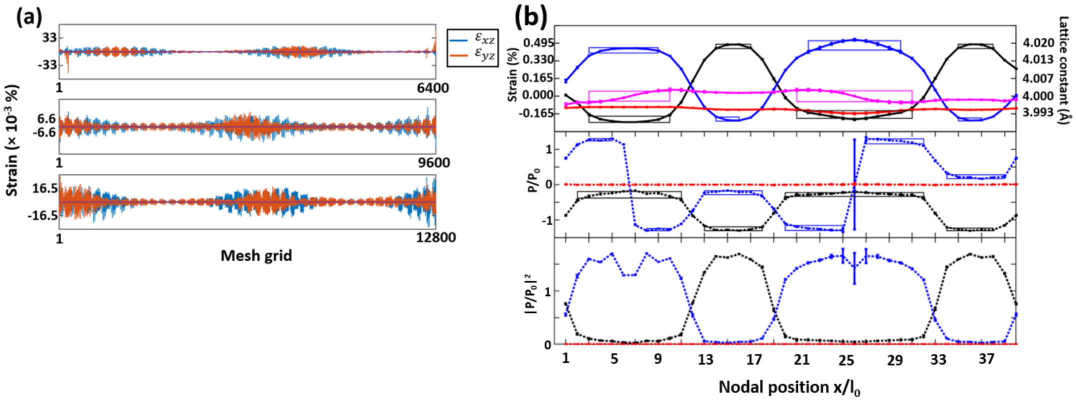

Fig. 5 (a) The values of shear strain ε_{xz} and ε_{yz} of all nodes in size I (6400 nodes), size II (9600 nodes), size III and IV (12800 nodes) simulations, respectively. The average values of the whole cell are $\varepsilon_{xz} = \varepsilon_{zx} = 0.0$ and $\varepsilon_{yz} = \varepsilon_{zy} = 0.0$ in all three sizes. (b) Data of strain tensor elements (ε_{xx}, ε_{yy}, ε_{xy} and ε_{zz}), polarization vectors and polarization magnitude square of the second grid plane in size I. The virtual scanning plane size is 40l_0 along x and 8l_0 along z. We plot the data along x direction, while the z direction variation is depicted by the error bar. The color scheme follows Fig. 3(c).

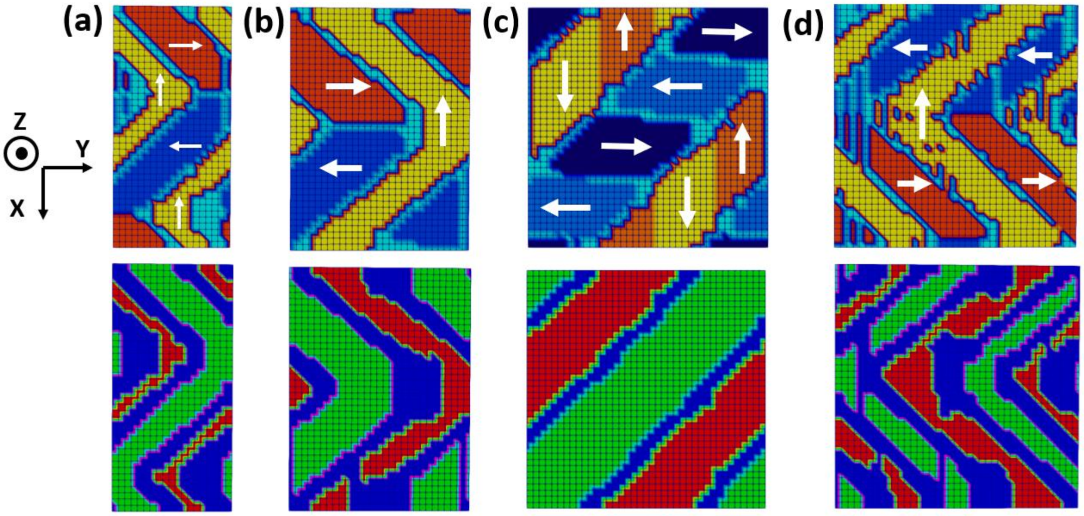

Fig. 6 Size I to IV from (a) to (d), respectively. The top panels of (a) to (d) are polarization distributions, where dark blue and black are P_y domains, orange and yellow are P_x domains, and cyan is the transition area. The polarization directions are depicted by white arrows. The bottom panels are crystallographic distributions. Color meanings follow Fig. 4.

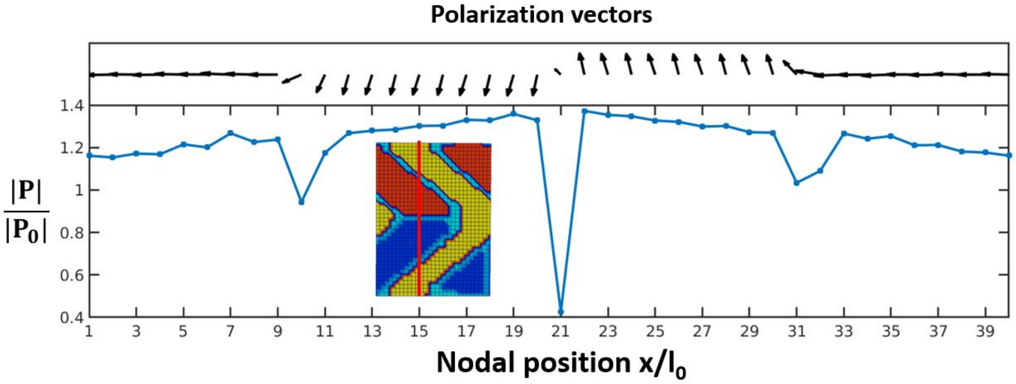

Fig. 7 The polarization vectors and their magnitudes in the scanning plane indicated by the red line from the $40l_0 \times 30l_0 \times 8l_0$ simulation cell. The polarization vector rotations are all in-plane because the P_z component is always zero in our results.

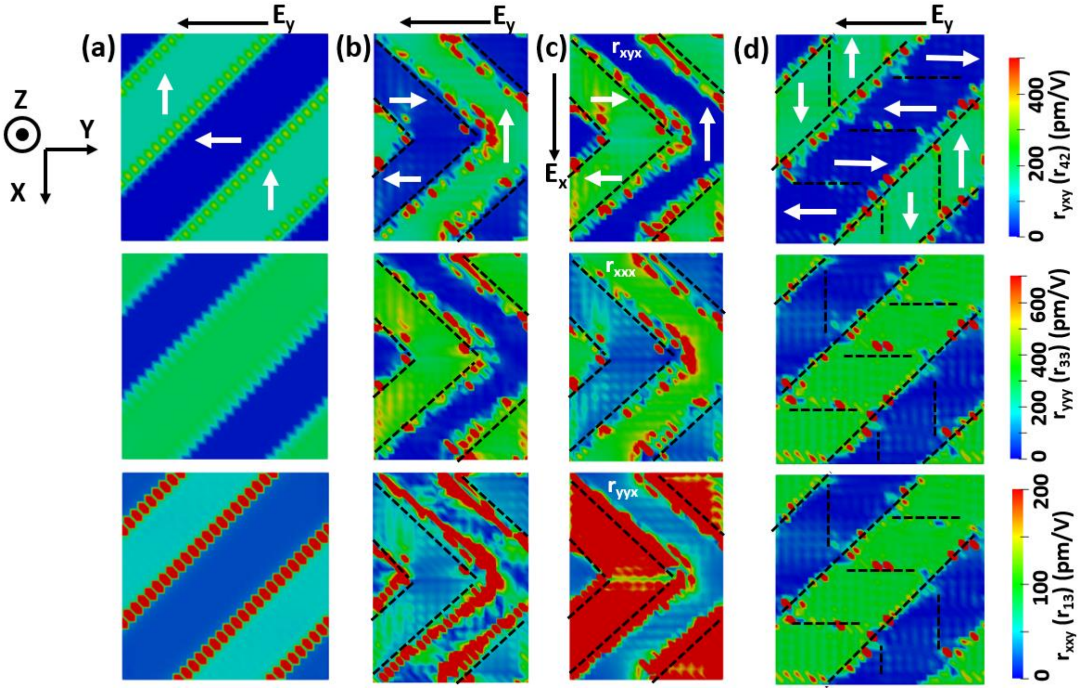

Fig. 8 Unclamped Pockels coefficient (r_{13}, r_{33} and r_{42}) morphologies. (a) Morphology corresponding to domain morphology from Fig. 4(b). (b)-(c) Morphology corresponding to domain morphologies from Fig. 6(b). (d) Morphology corresponding to domain morphologies from Fig. 6(c). The black dashed lines are used to highlight the DWs in the PFSs. The white arrows indicate the orientation of the domains. The black arrows are applied electric field direction.

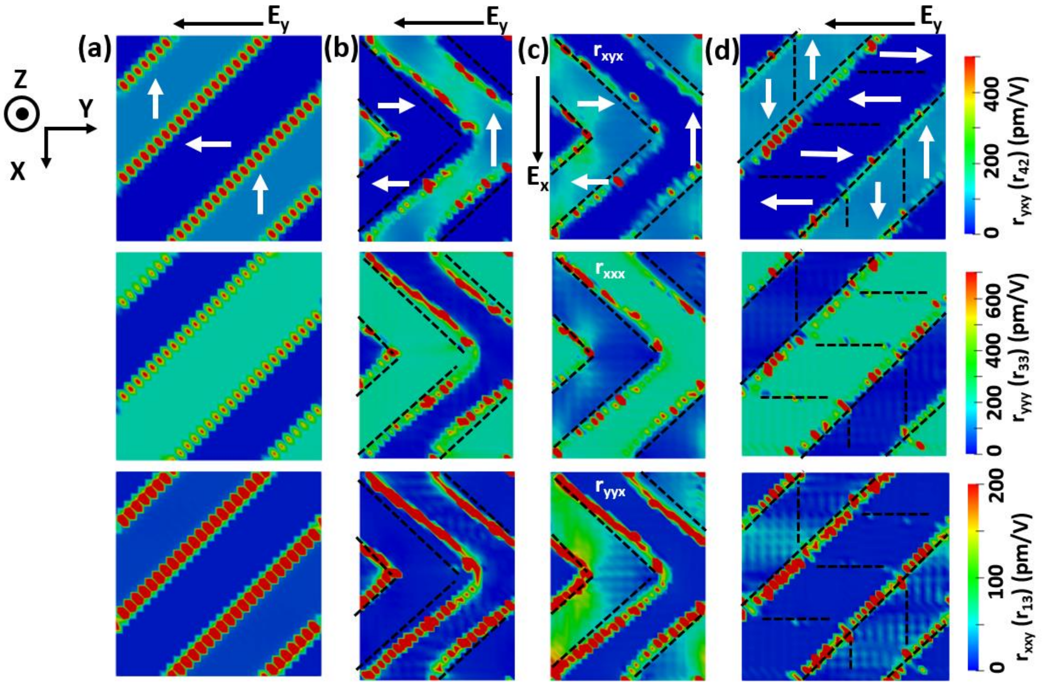

Fig. 9 Clamped Pockels coefficient (r_{13}, r_{33} and r_{42}) morphologies. Simulation cells from (a) to (d) are the same as Fig. 8.

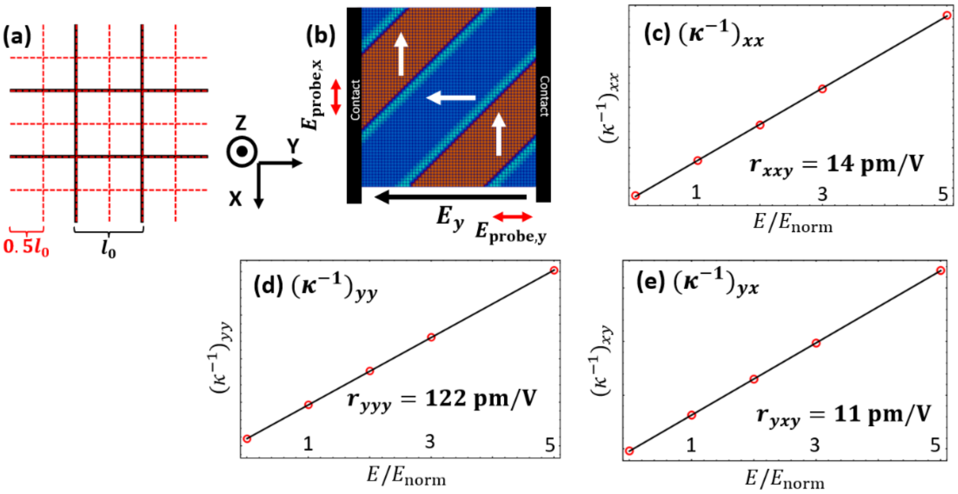

Fig. 10 (a) Schematic of the doubling of the fineness of the mesh. The total area (or volume in three dimensions) is kept the same. The black lines is the original grid, while the red lines correspond to that of the grid twice as fine. (b) Schematic of the setup to compute the Pockels tensor numerically. Two black rectangles represent metal contacts. The black arrow is the external electric field induced by the contacts, which is the field in the $r_y(E)$ term. The red arrows are the small perturbation field ($E_{probe} = 0.01E_{norm} \ll E_y$), used to detect the dielectric tensor under the external electric field. (c)-(e) are linear fits of each dielectric tensor element and the slopes are the Pockels coefficients. And $E_{norm} = 3.2 \times 10^4 (V/m)$.